JOURNAL OF GEOPHYSICAL RESEARCH, VOL. 101, NO. C6, PAGES 13,993–14,010, JUNE 15, 1996

Dynamics of the East India Coastal Current 2. Numerical solutions

J. P. McCreary and W. Han
Oceanographic Center, Nova Southeastern University, Dania, Florida

D. Shankar[1]
Centre for Mathematical Modelling and Computer Simulation, National Aerospace Laboratories Bangalore, India

S. R. Shetye
National Institute of Oceanography, Dona Paula, Goa, India

Abstract. A linear, continuously stratified model is used to investigate the dynamics of the East India Coastal Current (EICC). Solutions are found numerically in a basin that resembles the Indian Ocean basin north of 29°S, and they are forced by *Hellerman and Rosenstein* [1983] winds. Effects due to the following four forcing mechanisms are isolated: local alongshore winds adjacent to the east coasts of India and Sri Lanka, remote alongshore winds adjacent to the northern and eastern boundaries of the Bay, remotely forced signals propagating from the equator, and interior Ekman pumping. Each process contributes significantly to the EICC surface flow at some locations and at some times during the year. Along the Indian coast (north of 10°N), the surface EICC flows northeastward from February until September, with a strong peak in March-April and weaker flow from June to September; interior Ekman pumping, remote alongshore winds and equatorial forcing all contribute to the springtime peak, whereas local alongshore winds are the primary driving force of the weaker summertime flow. Along Sri Lanka (south of 10°N) the surface EICC flows northward only during March and April; the absence of northward flow at other times is due to interior Ekman pumping which drives a strong southward current for much of the year (April to December). Along both coasts there is southward flow from October to January that is driven by interior Ekman pumping and local alongshore winds. The EICC also has significant subsurface flow on several occasions. Along the Indian coast, there is southwestward flow extending to depths greater than 1000 m from May to July that is driven primarily by equatorial forcing. From July to September the southwestward flow forms a shallow subsurface counterflow (a Coastal Undercurrent); its cause is primarily equatorial forcing and interior Ekman pumping, not the local alongshore winds, as might be expected.

1. Introduction

Four different processes have been proposed as possible driving mechanisms of the East India Coastal Current (EICC): Ekman pumping in the interior of the Bay of Bengal [*Shetye et al.*, 1993], "local" alongshore winds adjacent to the east coasts of India and Sri Lanka [*McCreary et al.*, 1993], "remote" alongshore winds adjacent to the northern and eastern boundaries of the Bay [*McCreary et al.*, 1993], and remote forcing from the equator [*Yu et al.*, 1991; *Potemra et al.*, 1991]. Effects due to the first two mechanisms are investigated in detail by *Shankar et al.* [this issue], the companion paper to this one. In that study, analytic solutions are found to an approximate (essentially quasi-geostrophic) version of a linear, continuously stratified model in a basin confined to the Bay of Bengal. The advantage of this approach is that the mathematical structure of the analytic solutions clearly illustrates the fundamental physics of the system; however, the approach cannot be used to examine the latter two mechanisms because Rossby waves that radiate from the eastern boundary of the basin are distorted in the approximate system.

[1]Now at National Institute of Oceanography, Dona Paula, Goa, India.

Copyright 1996 by the American Geophysical Union.

Paper number 96JC00560.
0148-0227/96/96JC-00560$09.00

In this paper we investigate the influence of all four mechanisms by obtaining numerical solutions to the unapproximated version of the *Shankar et al.* [this issue] model in a basin that includes all of the Indian Ocean north of 29°S. The dynamics of the numerical solutions are not as transparent as they are in the analytic ones. However, because the model is linear, we are able to separate cleanly the complete response into a set of four "process solutions," each of which is forced by only a single forcing mechanism; this separation allows the contribution of each process to the EICC to be assessed quantitatively. Somewhat surprisingly given the dynamical simplicity of the model, our main-run solution compares favorably with observations in many regions of the Indian Ocean (for example, as in the comparison in Figure 4), and it is remarkably similar to the Indian Ocean solutions of more complex, nonlinear systems (such as those of *Anderson et al.* [1991] and *McCreary et al.* [1993]). This good agreement gives us confidence that the model properly represents fundamental dynamics of the large-scale circulations both within and outside the Bay.

2. Model Ocean

2.1. Equations of Motion

The model is described in detail elsewhere [*McCreary*, 1980, 1981; *Shankar et al.*, this issue], and so only aspects of the model essential to the present discussion are summarized here. The equations of motion are linearized about a background state of rest with Brünt-Väisälä frequency $N_b(z)$, and the ocean bottom (at $z = -D$) is assumed flat. With these restrictions, solutions can be represented as expansions in the vertical normal modes of the system, which are the eigenfunctions $\psi_n(z)$ of

$$\left(\frac{1}{N_b^2}\psi_{nz}\right)_z = -\frac{1}{c_n^2}\psi_n \tag{1}$$

subject to boundary conditions $\psi_{nz}(0) = \psi_{nz}(-D) = 0$, and the eigenvalues c_n are the Kelvin-wave speeds for each mode n. The expansions for the zonal velocity u, meridional velocity v, and pressure field p are

$$u = \sum_{n=1}^{N} u_n\psi_n, \tag{2a}$$

$$v = \sum_{n=1}^{N} v_n\psi_n, \tag{2b}$$

$$p = \sum_{n=1}^{N} \bar{\rho}\, p_n\psi_n, \tag{2c}$$

where the coefficients, u_n, v_n, and p_n are functions only of x, y, and t. In principle, the summations should extend to infinity, but solutions converge rapidly enough with n for the series to be truncated at a small value of N [see *Shankar et al.*, this issue]. The barotropic mode ($n = 0$) is not included in the sums because its contributions to current and sea level fields are small in comparison to those of the baroclinic modes [*Shankar et al.*, this issue]. For convenience, a factor of $1/\bar{\rho}$, where $\bar{\rho}$ is a typical value for the density of seawater, is absorbed into the definition of p_n, and with this choice p_n has units of velocity squared.

The resulting equations for the expansion coefficients are

$$u_{nt} - fv_n + p_{nx} = F_n - \frac{A}{c_n^2}u_n + \nu_2\nabla^2 u_n - \gamma u_n - \delta u_n, \tag{3a}$$

$$v_{nt} + fu_n + p_{ny} = G_n - \frac{A}{c_n^2}v_n + \nu_2\nabla^2 v_n, \tag{3b}$$

$$\frac{p_{nt}}{c_n^2} + u_{nx} + v_{ny} = -\frac{A}{c_n^4}p_n - \frac{\delta}{c_n^2}p_n, \tag{3c}$$

where $f = \beta y$ is the Coriolis parameter and ν_2 is the horizontal mixing coefficient. Forcing by the wind is introduced as a body force with a vertical profile $Z(z)$, resulting in the terms $F_n = \tau^x \mathcal{Z}_n/(\bar{\rho}\mathcal{H}_n)$, $G_n = \tau^y \mathcal{Z}_n/(\bar{\rho}\mathcal{H}_n)$, where τ^x and τ^y are zonal and meridional components of the wind stress, and $\mathcal{H}_n = \int_{-D}^{0} \psi_n^2 dz$ and $\mathcal{Z}_n = \int_{-D}^{0} Z(z)\psi_n(z)dz$ are coupling factors (see section 2.3). The system has vertical mixing with the coefficient $\nu = A/N_b^2$, resulting in the terms proportional to A. As discussed next, all solutions have a damper with coefficient $\gamma(y)$ near the southern boundary of the basin, and the test solutions also include a damper with coefficient $\delta(x, y)$ in the eastern equatorial ocean.

2.2. Boundary Conditions and Dampers

Solutions are found in a basin that resembles the actual Indian Ocean. Its shape in the Bay of Bengal is shown in Figures 1, 2, and 5. The entire basin is shown in *McCreary et al.* [1993].

The southern boundary of the model does not coincide with any real boundary of the Indian Ocean, and we apply the zero-gradient, open boundary conditions,

$$u_{ny} = v_{ny} = p_{ny} = 0, \tag{4}$$

there. The condition $u_{ny} = 0$ allows the development of a large-scale instability along the boundary, and the damper with coefficient $\gamma(y)$ is required to inhibit its growth. The damper is present only very near the southern boundary, with γ having a value of 1 day^{-1} within 150 km of the boundary, and decreasing to zero linearly in the interval from 150 km to 300 km. There is no corresponding damper on v_n and p_n, so that fluid can pass freely through the open boundary.

Two sets of boundary conditions are applied along continental barriers. One set is

$$u_n = v_n = 0, \tag{5a}$$

the usual, closed, no-slip conditions. The other set,

$$\tilde{u}_n = \mathbf{n}\cdot\mathbf{v}_n = -\mathbf{n}\cdot\mathbf{k}\times\frac{\mathbf{F}_n}{f}, \qquad \tilde{v}_n = \mathbf{k}\times\mathbf{n}\cdot\mathbf{v}_n = 0, \tag{5b}$$

is applied to the boundaries of the Bay for two of the test solutions (section 2.4); in the above, $\mathbf{n}$ is a unit vector normal to the boundary that points into the Bay along its western and northern sides and points out of the Bay on its northeastern and eastern sides, $\mathbf{k}$ is a unit vector directed upward, $\mathbf{v}_n = (u_n, v_n)$, $\tilde{u}_n$ and $\tilde{v}_n$ are velocity components perpendicular and parallel to the boundary, and $\mathbf{F}_n = (F_n, G_n)$. Conditions (5b) allow Ekman flows to pass through boundaries, and therefore circulations by coastal Ekman pumping are filtered out of solutions. (Throughout this paper we use the phrase "forcing by alongshore winds" to denote "forcing by coastal Ekman pumping." A precise, mathematical definition of the response forced by alongshore winds at the western boundary of the Bay is provided by *Shankar et al.* [this issue, equation (32c)]).

The damper with coefficient $\delta(x, y)$ is nonzero only in the eastern equatorial ocean within the region $x >$ 92.75°E, $-7.5°\text{S} < y < 7.5°\text{N}$. In this region, δ has a maximum value of $c_n/(1.5\Delta x)$, where Δx is the zonal grid step, and it decreases linearly to zero within 5° of its western edge and within 2° of its northern and southern edges. This damper causes equatorial Kelvin waves to decay rapidly in an e-folding scale of 1.5 Δx and therefore isolates circulations within the Bay from effects due to equatorial forcing. We have carried out a series of tests to investigate the sensitivity of solutions to the meridional extent of the damper; the process solutions in section 3.2 are virtually unchanged when the location of the northern edge of the damper is varied from 5°N to 8.5°N.

2.3. Forcing, Parameters, and Numerics

The model is forced by the climatological winds of *Hellerman and Rosenstein* [1983], linearly interpolated onto the numerical grid. Figure 1 shows the wind-stress vectors $\boldsymbol{\tau}$ and the Ekman pumping velocity $\mathcal{E} = (1/\bar{\rho})\text{curl}(\boldsymbol{\tau}/f)$ from this data set.

Model parameters are the same as those used by *Shankar et al.* [this issue]. The background Brünt-Väisälä frequency $N_b(z)$ is the profile used by *Moore and McCreary* [1990], and the depth of the ocean D is 4000 m. Solutions do not appear to be sensitive to this choice of $N_b(z)$; in a test solution with $N_b(z)$ determined using the average density field in the Bay from the *Levitus* [1982] data, the resulting flow field was very similar to that of our main run in both structure and amplitude. The assumed body-force profile $Z(z)$, defined precisely by *Shankar et al.* [this issue, equation (8)], is constant for $z > -50$ m and ramps to zero in the depth range -100 m $< z \leq -50$ m. The number of modes used in summations (2a)–(2c) is $N = 10$, and solutions are well converged with this choice when $Z(z)$ is ramped. Other model parameters are $\beta = 2.28\times10^{-13}$ cm^{-1} s^{-1}, $A = 1.3\times10^{-4}$ cm^2 s^{-3} and $\nu_2 = 5\times10^7$ cm^2 s^{-1}; solutions are not sensitive to the value of A [*Shankar et al.*, this issue], and ν_2 is set to a value large enough to ensure numerical stability. A number of quantities associated with individual vertical modes are given by *Shankar et al.* [this issue, Table 1].

Solutions are found numerically on a staggered grid, with variables defined in rectangular boxes of dimension $\Delta x = \Delta y = 55$ km; p_n points are located at the center of the boxes, whereas u_n and v_n points are located on their meridional and zonal edges, respectively. Equations (3a)–(3c) are integrated forward in time, using the leap frog scheme with a time step $\Delta t = 1.5$ hours. To inhibit time-splitting instability, the fields are averaged between successive time levels every 41 time steps. Diffusive terms are evaluated at the backward time level, and all other terms at the central time level. Integrations are all started from a state of rest beginning on April 15, a time during the transition between the monsoons when the winds are weak. The solutions shown in the figures are taken from the fourth year of the integration, by which time the circulation in the Bay of Bengal has approached stationarity.

2.4. Main-Run and Process Solutions

Our main-run solution (MR) is the one that results when boundary conditions (5a) are used and there is no equatorial damper (i.e., $\delta \equiv 0$). The process solutions that isolate the contributions of each of the four forcing mechanisms are determined from the main run and three test calculations (referred to as solutions 1-3). All three tests include the equatorial damper and therefore filter out effects due to equatorial forcing from the response in the Bay of Bengal. Solution 1 differs from the main run only because of this damper. Solution 2 also applies boundary conditions (5b) along the western boundary of the Bay (from 82°E, 6.5°N to 87°E, 20°N), and so removes effects driven by the alongshore winds (coastal Ekman pumping) adjacent to that boundary. Similarly, solution 3 applies (5b) along the northern and eastern boundaries of the Bay (from 87°E, 20°N to 97°E, 2.5°N) thereby eliminating effects due to the alongshore winds there. The process solutions forced only by equatorial forcing (EQ), local alongshore winds (LA), and remote alongshore winds (RA) are then given by EQ = MR − solution 1, LA = solution 1 − solution 2, and RA = solution 1 − solution 3. The solution driven only by Ekman pumping in the interior of the Bay (EP) is the response that remains when the other three process solutions are removed from the main run; that is, EP = MR − (EQ + LA + RA). Solutions LA and EP are the numerical analogs of the analytic solution discussed by *Shankar et al.* [this issue].

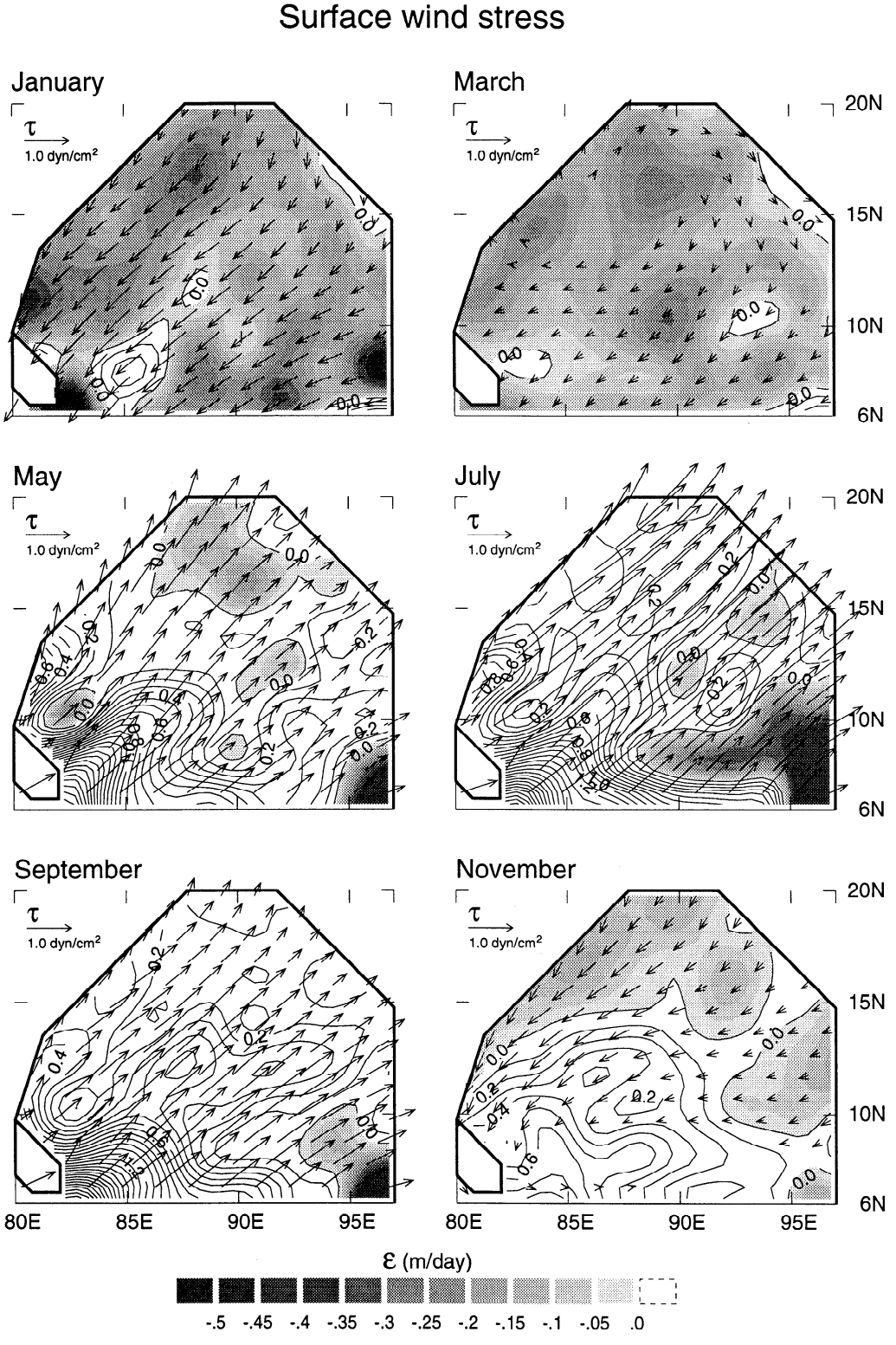

Figure 1. Bimonthly maps of wind stress τ and Ekman pumping velocity $\mathcal{E}$. Contour intervals for $\mathcal{E}$ are 0.1 $\mathrm{m\,d^{-1}}$ for positive values and 0.05 $\mathrm{m\,d^{-1}}$ for negative values; negative values are indicated with a graduated gray scale. From November through April, $\mathcal{E}$ is negative throughout the northern Bay of Bengal. From April through October, $\mathcal{E}$ is strong and positive in the southwestern basin.

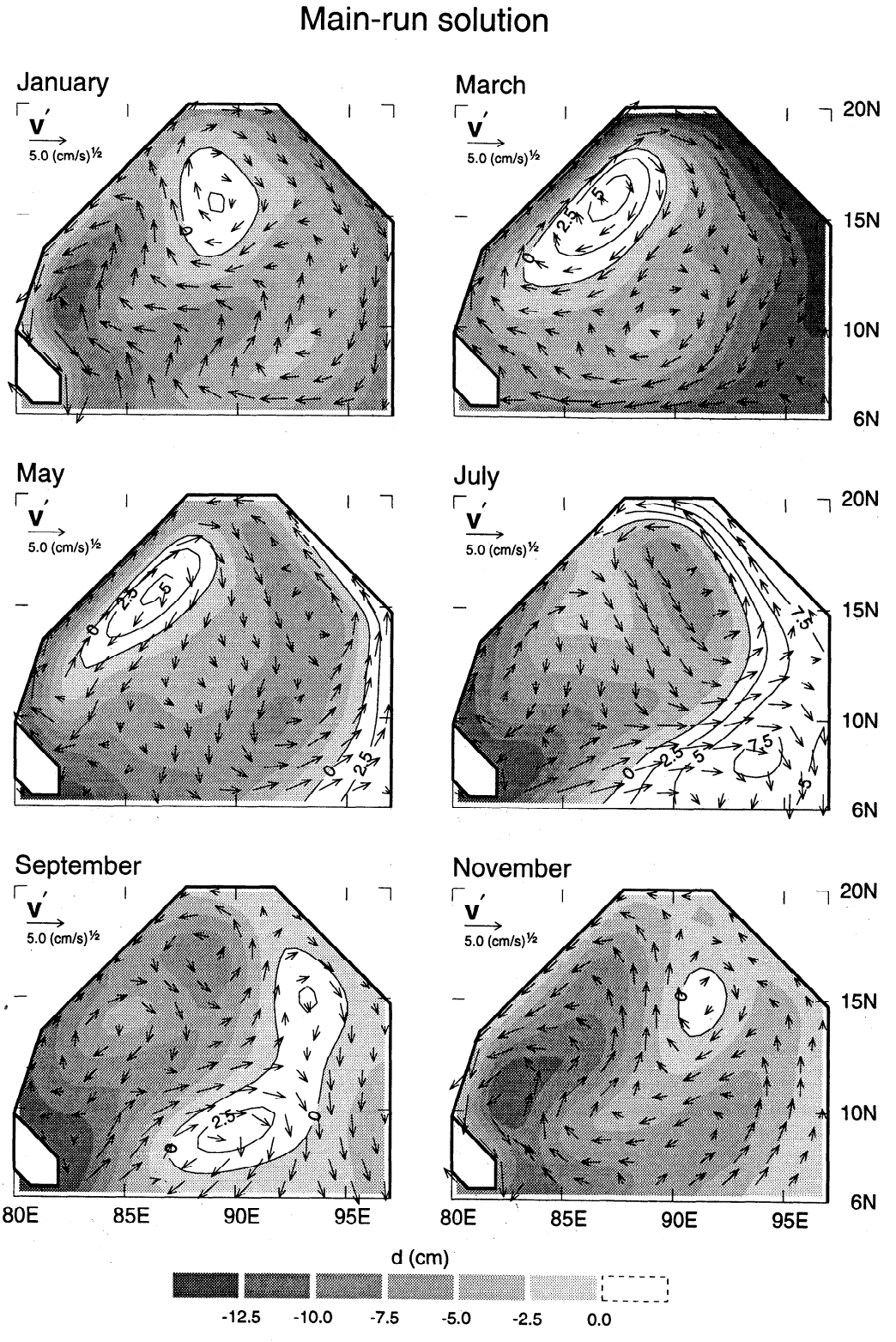

Figure 2. Bimonthly maps of surface currents $\mathbf{v}$ and dynamic height d for the main run. The contour interval for d is 2.5 cm, and negative values are indicated with a graduated gray scale. To emphasize the weaker flows, current arrows are of the vector field $\mathbf{v}' = \mathbf{v}/|\mathbf{v}|^{1/2}$. In January an anticyclonic gyre develops in the northern Bay. By March there is a well-developed anticyclonic circulation throughout most of the Bay and a strong northeastward EICC. From May through September, d is high in the eastern basin, low in the southwestern region, and d slopes downward to the south along the Indian coast; current arrows cross isolines of d due to the intensity of the Ekman drift. In November, d increases everywhere along the coasts of India and Sri Lanka to its value in the northern basin, resulting in a swift southward coastal current.

3. Results

In section 3.1 we describe the annual cycle of our main-run solution. Then, in section 3.2 we describe the distinctive circulations present in each of the process solutions. Finally, in section 3.3 we discuss how each process solution contributes to the model EICC.

3.1. Model Annual Cycle

Figures 2-4 provide an overview of the main run. Figure 2 presents bimonthly maps illustrating the horizontal structures of the surface flow field, $\mathbf{v} = \sum_{n=1}^{N} \mathbf{v}_n$, and the surface dynamic height field, $d = \sum_{n=1}^{N} p_n/g$, where g is the acceleration of gravity. Figure 3 provides depth-time plots of the EICC alongshore flow, $\tilde{v} = \sum_{n=1}^{N} \tilde{v}_n \psi_n(z)$, at 16°N and 12°N along the Indian coast and 8°N off Sri Lanka; the currents are evaluated off the coast at the position where the surface flow attains its maximum amplitude ($\sim$ 80 km offshore). Among other things, Figure 3 shows that the surface currents are spread relatively uniformly throughout a surface mixed layer, where $Z(z)$ is constant and $N_b(z)$ is close to zero, and that there are significant currents in the deep ocean. Figure 4 shows annual curves at 16°N, 12°N, and 8°N of the surface alongshore flow averaged across the EICC

$$\langle \tilde{v} \rangle = \sum_{n=1}^{N} \frac{1}{\Delta s} \int_0^{\Delta s} \mathbf{v}_n \times \mathbf{k} \cdot \mathbf{dl} = \sum_{n=1}^{N} \frac{1}{\Delta s} \int_0^{\Delta s} \tilde{v}_n ds \quad (6)$$

(thick curves), and EICC transport relative to 1000 m

$$\tilde{V} = \sum_{n=1}^{N} \left\{ \int_0^{\Delta s} \tilde{v}_n ds \int_{-H}^{0} [\psi_n(z) - \psi_n(-H)]\, dz \right\} \quad (7)$$

where H = 1000 m (dashed curves); in these definitions, Δs is the current width (essentially the width of a *Munk* [1950] layer), and $\mathbf{dl} = \mathbf{n} ds$ so that the line integral extends directly across the current.

Figure 4 also plots curves of EICC surface velocity from the ship-drift data compiled by *Rao et al.* [1989, 1991] (thin curves), and they compare remarkably well with the $\langle \tilde{v} \rangle$ curves from the solution. On the other hand, model transports tend to be weaker than observed estimates. For example, *Shetye et al.* [this issue] estimated the transport of the springtime northeastward EICC to be 10 Sv relative to 1000 m, whereas its maximum transport in the model is only 5 Sv (Figure 4); a possible reason for this discrepancy is that the observed estimate is based on data taken during a single year and so is not representative of the climatology. A possible dynamical reason is noted at the end of section 3.3.3.

3.1.1. Spring. At the surface the model EICC begins to flow northeastward along the Indian coast in the spring, against the winds of the Northeast Monsoon, reaching its maximum strength in April or May (Figures 3 and 4, top and middle). This development is not an isolated coastal response but, rather, takes

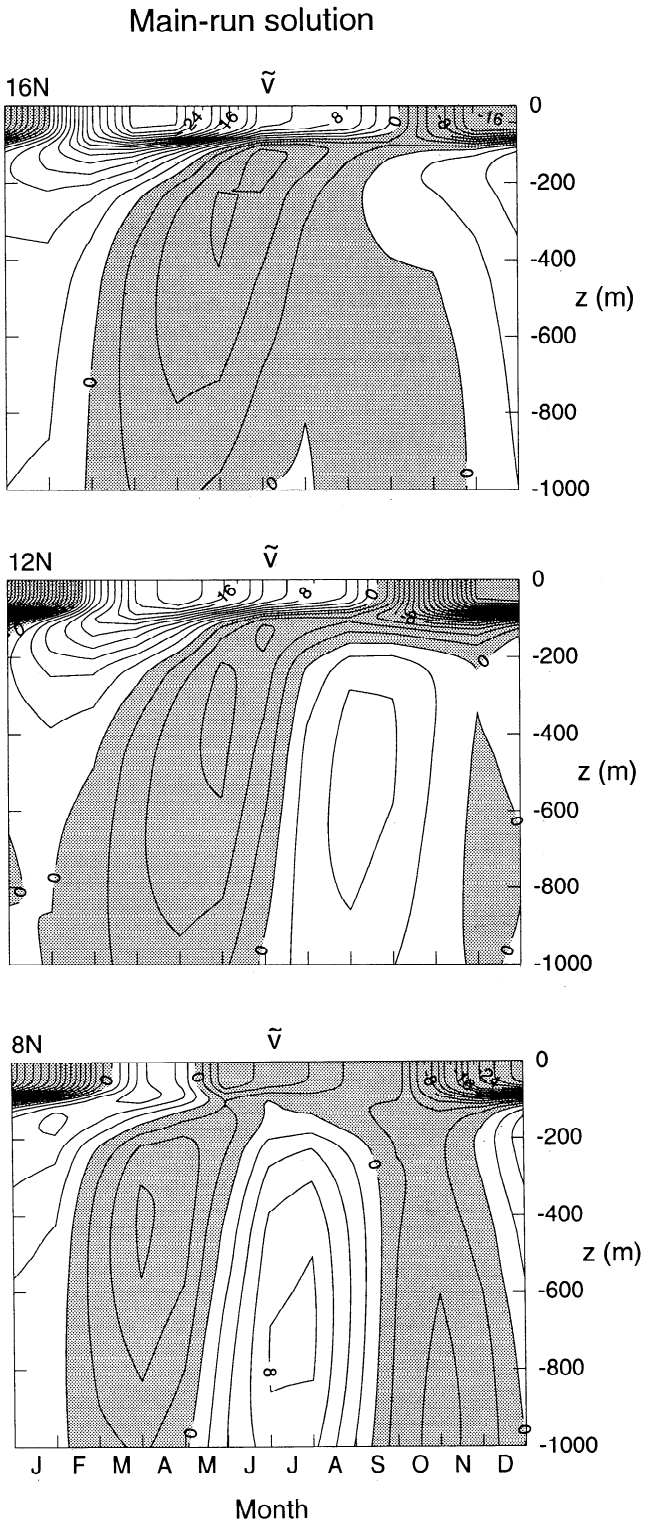

Figure 3. Depth-time plots of the alongshore current $\tilde{v}$ about 80 km offshore, where the current speed is a maximum at 16°N, 12°N, and 8°N. The contour interval is 2 cm s^{-1}, and regions of southward flow (negative values) are shaded. There are strong flows in the surface mixed layer ($z > -65$ m), and deep currents extend to depths below 1000 m. During the summer a subsurface counterflow (a Coastal Undercurrent) is present at 16°N and 12°N along the Indian coast. There is evidence of upward phase propagation, an indicator of remotely forced signals that are carrying energy downward.

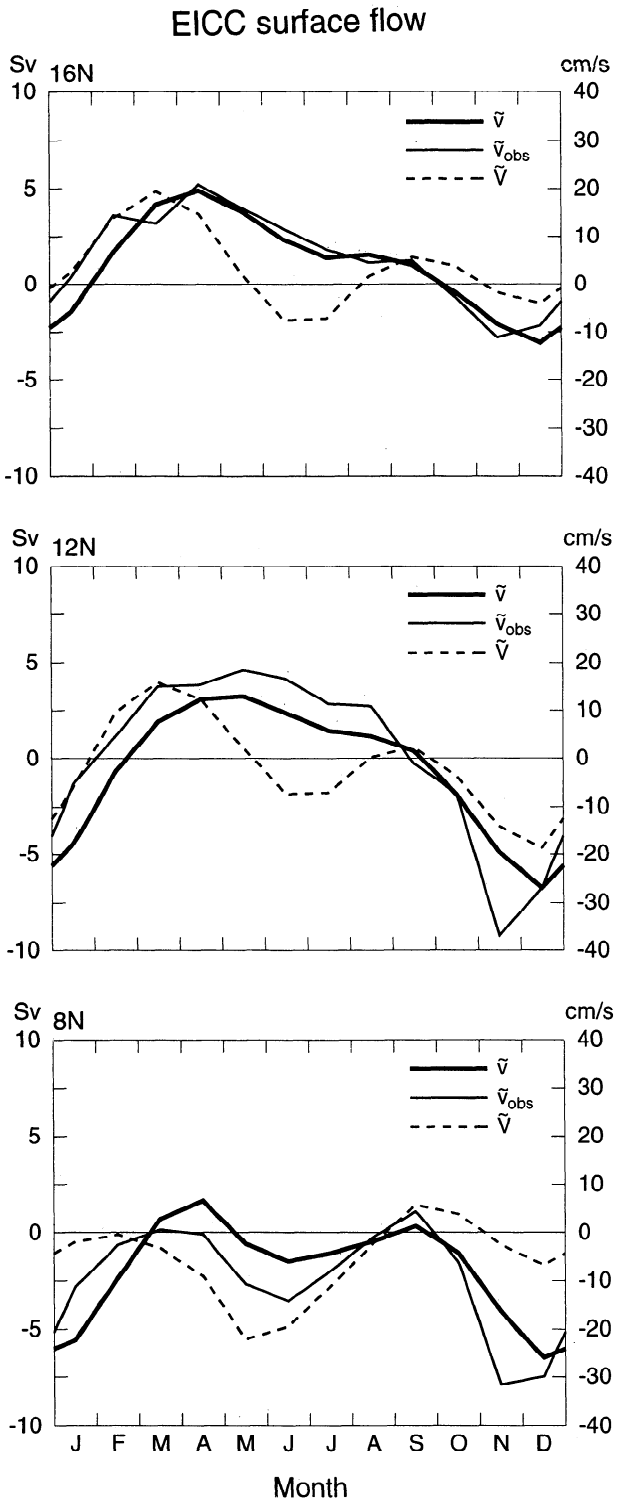

Figure 4. Time plots of the average surface velocity $\langle\tilde{v}\rangle$ (thick curves) and transport $\tilde{V}$ (dashed curves) for the model EICC, as well as the EICC surface velocity from the ship-drift data (thin curves), at 16°N, 12°N, and 8°N. The $\langle\tilde{v}\rangle$ field attains its maximum northward flow during the spring and its maximum southward flow during the winter. The transport field $\tilde{V}$ reverses direction during the summer at 16°N and 12°N along the Indian coast, a consequence of the deep southwestward flow present from March through June (Figure 3). The modeled and observed velocity fields are in good agreement at all three locations.

place in association with large-scale changes throughout the Bay. In January an anticyclonic gyre forms in the northern Bay, circulating about a region of positive d, and the EICC reverses to flow northeastward north of 17°N as the northwestern branch of this gyre. The gyre intensifies in February, and by March the EICC flows northeastward everywhere along the Indian coast. Also during this time, d decreases in the eastern basin and around the perimeter of the Bay due to equatorial forcing (section 3.2), resulting in southward flow in the eastern basin and intensified northeastward flow along the east coast of India; consequently, by March the EICC appears to be the northwestern branch of a basin-wide anticyclonic circulation, consistent with the observed flow field [*Shetye et al.*, 1993].

Figure 3 shows that the northeastward EICC appears first in November at a depth of about 200 m and subsequently propagates upward in the water column; this property suggests that part of this response consists of a remotely forced signal that is carrying energy downward, and this conclusion is confirmed in section 3.2. A similar upward propagation of northward flow is present at 8°N off Sri Lanka as well, but it does not generate a long-lasting, northward surface current.

3.1.2. Summer. The Southwest Monsoon begins in May and attains its peak strength in July. In response, d shallows markedly in a region off Sri Lanka and southern India, and by July there is a large slope in d along the Indian coast, downward toward the south (Figure 2, July). Because the local winds are so intense, one might expect the EICC to flow most strongly to the northeast at this time, but that is not the case; instead, along the Indian coast the EICC is considerably weaker than it was in the spring, and off Sri Lanka it is southward (Figures 3 and 4). As we shall see in section 3.3, one cause of the weakness along India is a remotely forced signal that appears in the eastern basin in May as a region of increased d and cyclonic flow and that intensifies and spreads westward in June and July (Figure 2); in July the cyclonic flow has spread around the perimeter of the basin to meet the northeastward EICC near 18°N. *Shetye et al.* [1991] noted a similar transition (from northeastward surface flow in the south to southwestward flow in the north) in the observed EICC structure, and it is also present in the solution of *McCreary et al.* [1993].

The subsurface structure of the EICC also changes considerably during this time. Along the Indian coast a region of southwestward flow appears in March at a depth of about 800 m; it propagates upward during May and June, and from June until September forms a shallow subsurface counterflow (Figure 3, top and middle). This shallow counterflow has a structure much like that of the Coastal Undercurrent typically present along eastern ocean boundaries but, as we shall see, its dynamics are considerably different (section 3.3). A similar Coastal Undercurrent also developed in the solution of *McCreary et al.* [1993], and there is evidence

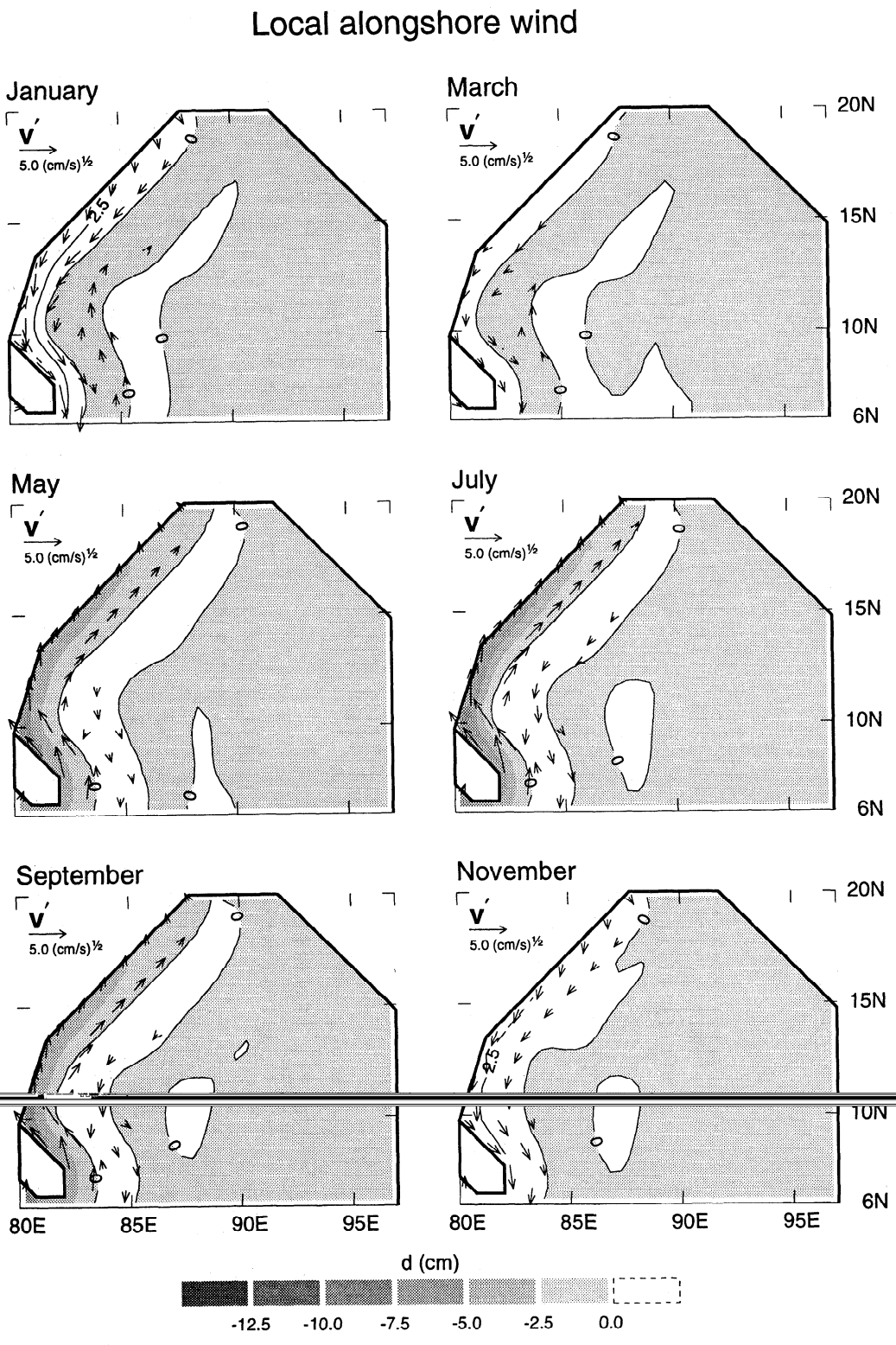

Figure 5a. Bimonthly maps of surface currents $\mathbf{v}$ and dynamic height d for the solution driven by local alongshore winds (LA). The contour interval for d is 2.5 cm, and negative values are indicated by a graduated gray scale. To emphasize the weaker flows, current arrows are of the vector field $\mathbf{v}' = \mathbf{v}/|\mathbf{v}|^{1/2}$. The strength and direction of the EICC closely follows the wind, its amplitude increases to the south, and the offshore current reversals are due to horizontal mixing. Dynamic height slopes along the coast to balance the wind stress, and there is geostrophic flow across the western boundary.

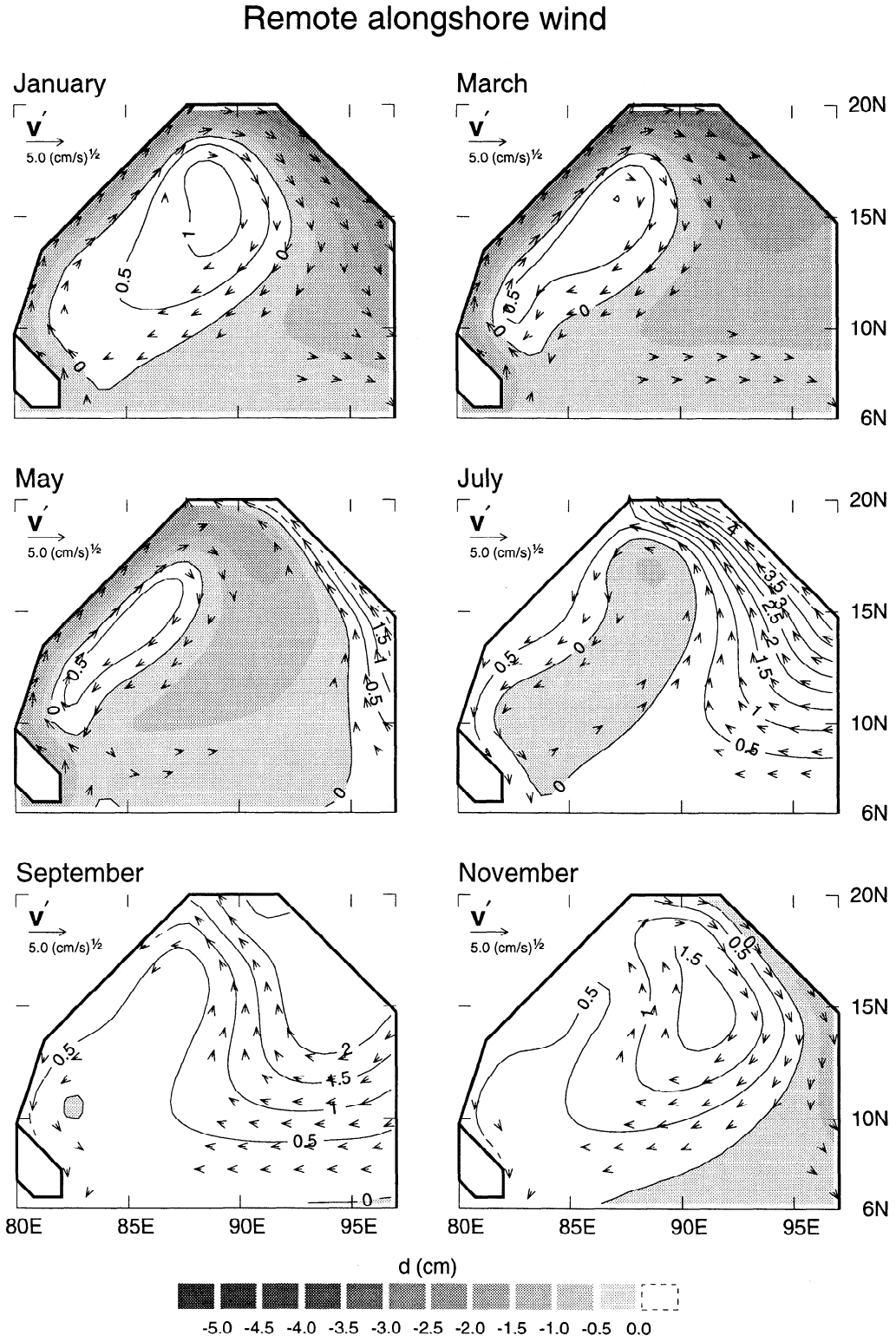

Figure 5b. Same as Figure 5a, except for the process solution driven by remote alongshore winds (RA) and the contour interval for d is 0.5 cm. From November through April, upwelling-favorable winds drive a geostrophic outflow from the eastern and northeastern boundaries of the Bay and a northeastward EICC. From May through September, downwelling-favorable winds drive an outflow across the eastern boundary and northward flow in the eastern basin; at the same time, upwelling-favorable winds along the northern boundary cause a geostrophic inflow along the northern boundary, thereby inhibiting the generation of a significant southwestward EICC during the Southwest Monsoon. Areas of positive and negative d propagate across the basin as Rossby waves.

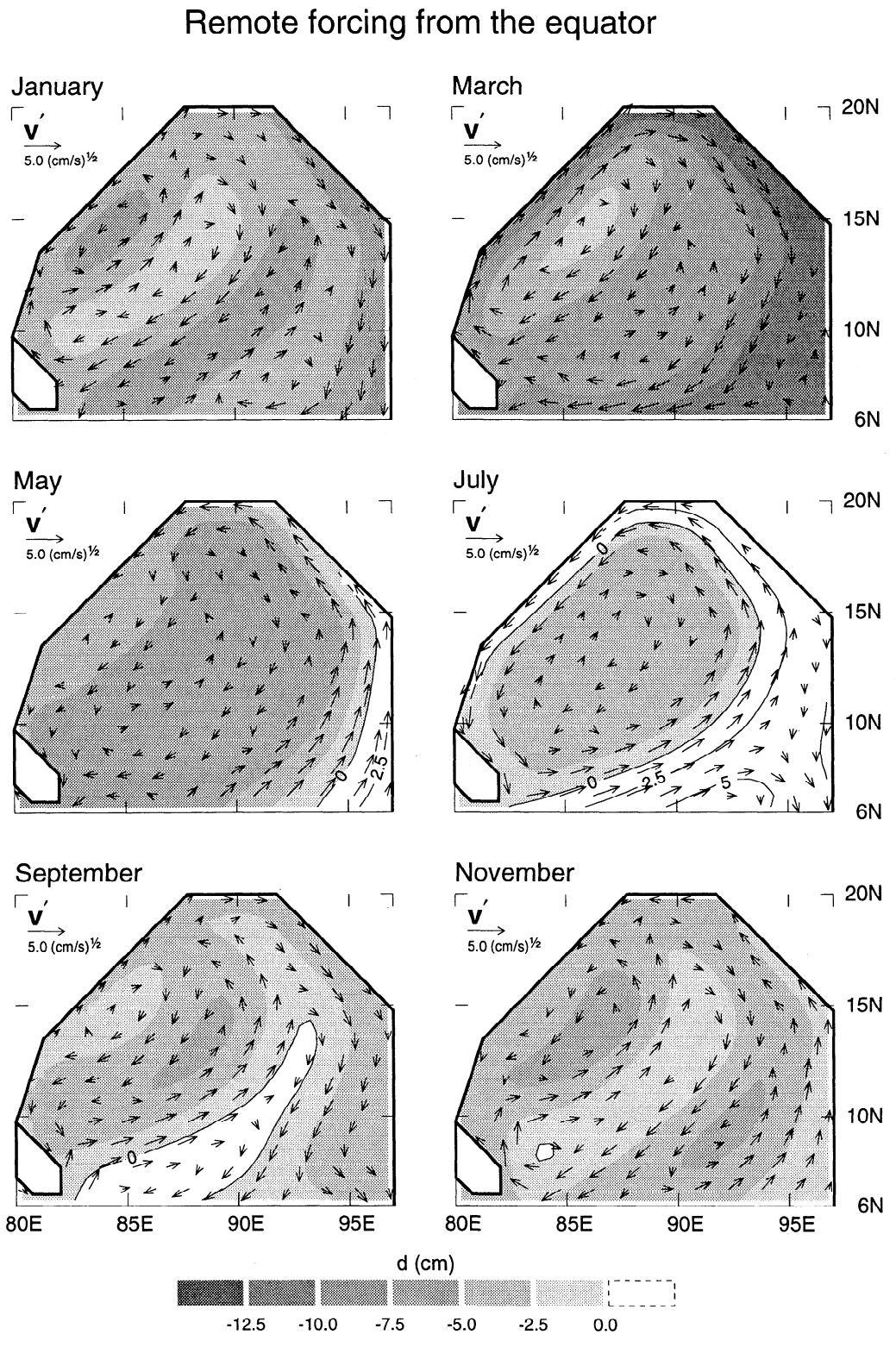

Figure 5c. Same as Figure 5a, except for the process solution driven by remote forcing from the equator (EQ). From January through March, d is shallow in the eastern basin and around the perimeter of the Bay and there is anticyclonic flow around the perimeter of the Bay. From April through July, d is high in the eastern basin and around the perimeter of the Bay and the flow along the Indian coast is cyclonic. A region of high d propagates across the basin as a packet of Rossby waves generating strong northward flow when it arrives at the coast of Sri Lanka.

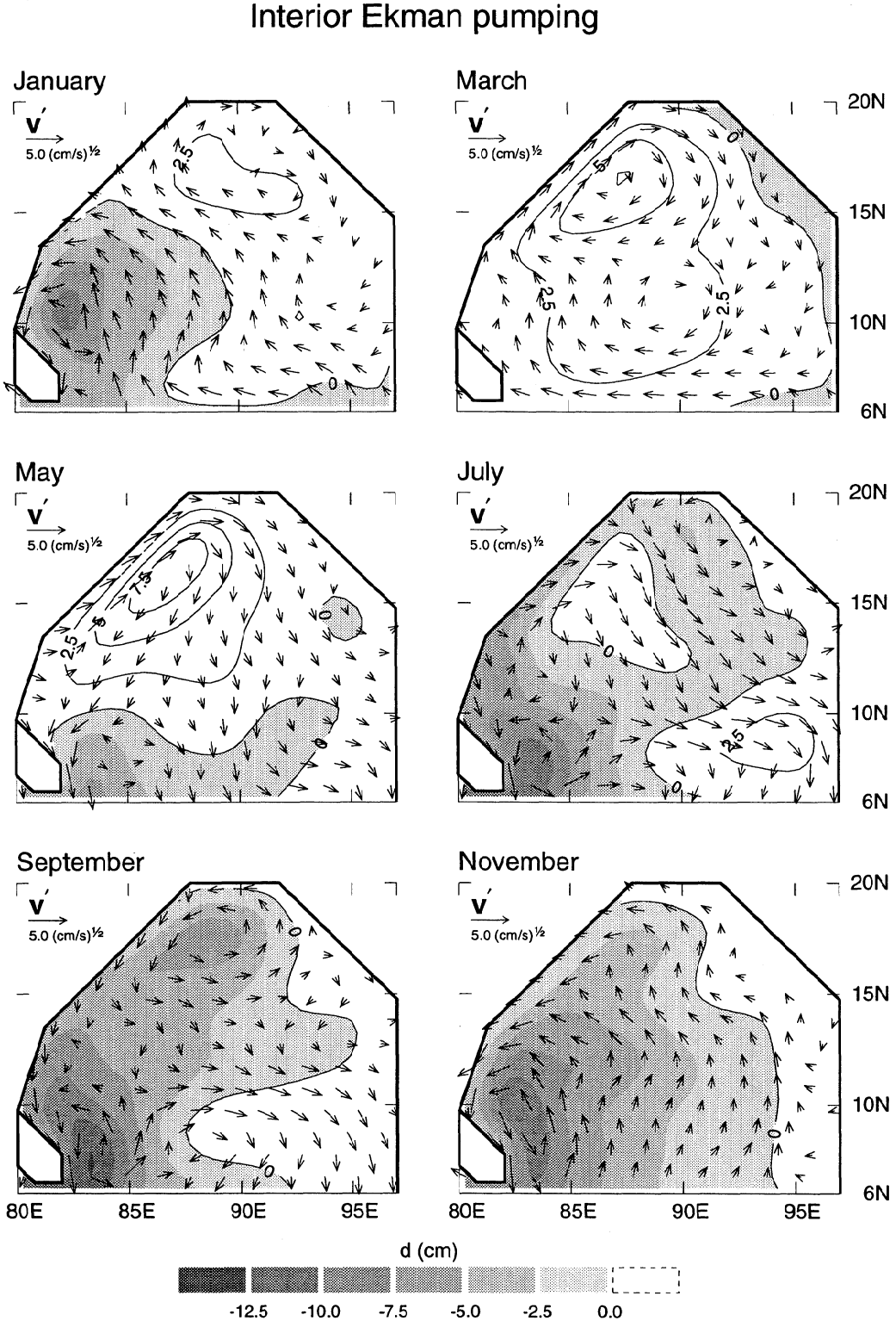

Figure 5d. Same as Figure 5a, except for the process solution driven by Ekman pumping (EP). From November through April, d increases in the northern Bay due to $\mathcal{E}$ being negative there (Figure 1) and there is anticyclonic flow around this region. From May through December, d decreases in the southwestern basin due to positive $\mathcal{E}$ and there is cyclonic flow there.

that such a flow also exists in the real ocean [*Shetye et al.*, 1991]. Although current speeds associated with the deep flow are not large, they do have a significant effect on the EICC transport; indeed, they are the reason that the EICC transport reverses to flow southwestward during the summer, whereas the surface current does not (Figure 4, top and middle). The existence of this subsurface flow and its effect on the EICC transport have also been inferred by S. K. Behera and P. S. Salvekar (unpublished manuscript, 1995).

3.1.3. Fall and winter. In September the Southwest Monsoon weakens to about half its July strength (Figure 1). Generally, prominent aspects of the circulation are still similar to those in July (Figure 2, September). One obvious difference, however, is that d has dropped in the eastern basin since July. As a consequence, the region of positive d adjacent to the eastern boundary in May and July is now located offshore. This region continues to propagate westward as a Rossby wave and weakens throughout the year (Figure 2, November and January), eventually reaching the western boundary in March, when it contributes to the anticyclonic circulation there.

The Southwest Monsoon collapses in October, and the winds shift to northeasterly in November (Figure 1). Because there is no wind stress to maintain the dynamic-height slope along the Indian coast, d adjusts to its value in the northern Bay everywhere along the coast, and the EICC responds by reversing to flow swiftly to the southwest (Figure 2, November). Interest-

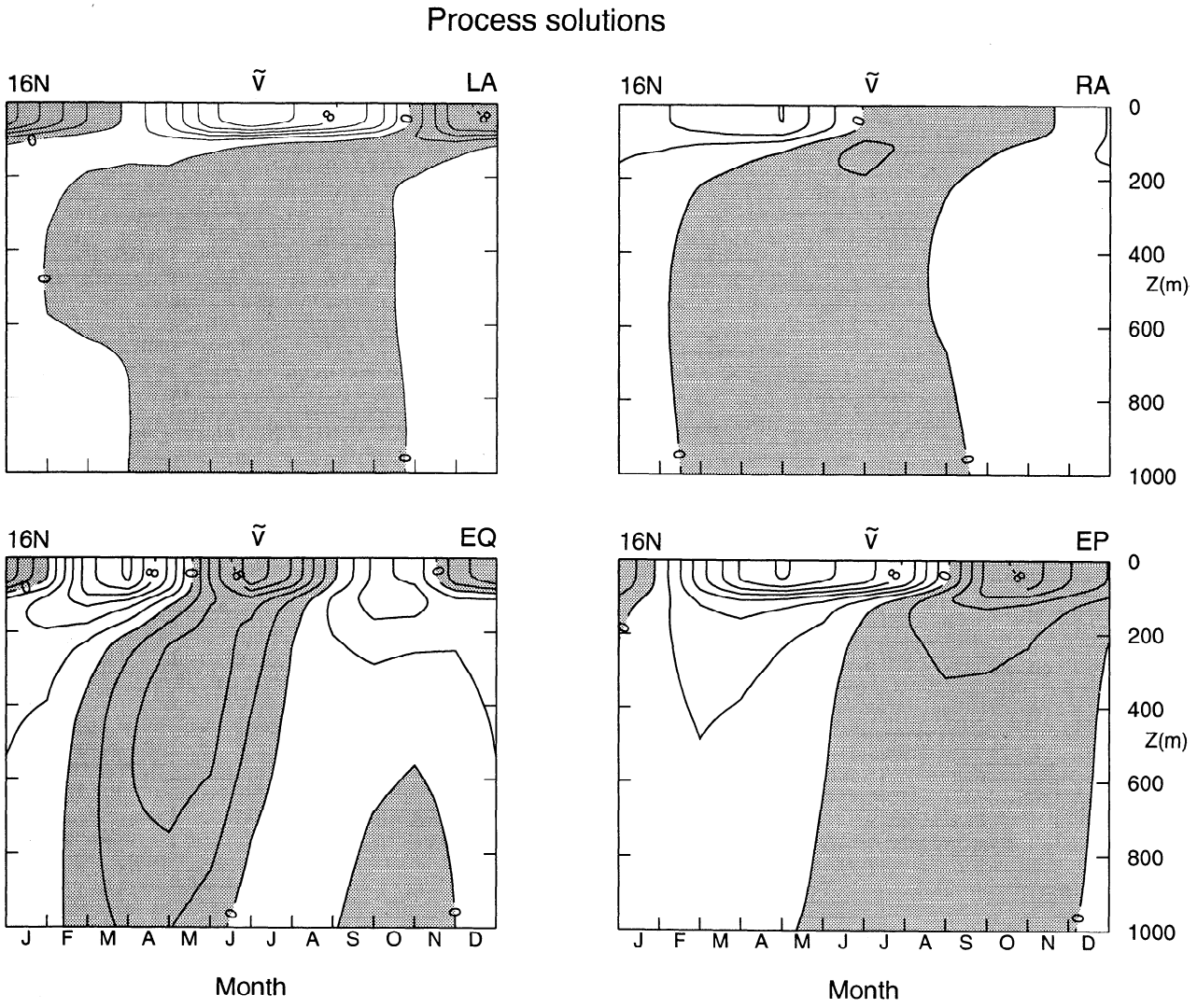

Figure 6a. A depth-time plot showing the contribution of each process solution to the alongshore flow about 80 km offshore at 16°N. Solution LA (top left) is confined largely to the surface mixed layer, with only weak subsurface counterflows. Solution RA (top right) is also confined largely to the mixed layer; it is associated with strong northeastward flow during the winter but only weak southwestward flow during the summer. Solution EQ (bottom left) has strong deep currents that extend to 1000 m, and there is evidence of vertical phase propagation; the semiannual component of this solution is visually stronger than it is for the other process solutions. Solution EP (bottom right) also has deep currents and evidence of vertical phase propagation.

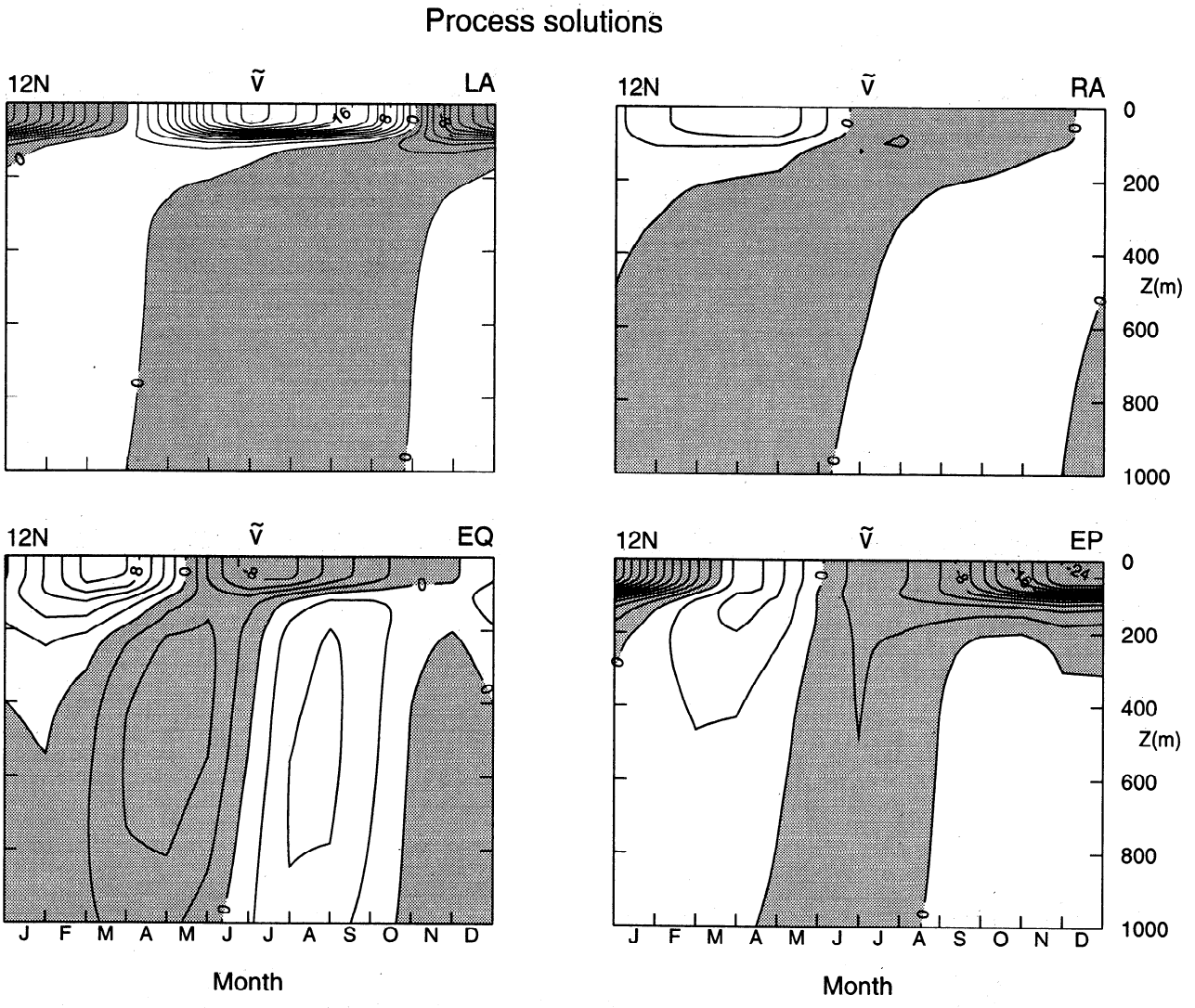

Figure 6b. Same as Figure 6a, except at 12°N. In contrast to their counterparts at 16°N (Figure 6a), solution LA has a larger amplitude, solution RA is somewhat weaker, and solution EP has considerably less northeastward surface flow.

ingly, this current extends around the tip of India via Kelvin-wave propagation, where it generates a strong northwestward current along the west coast of India (see the discussion by *McCreary et al.* [1993]). The southwestward EICC reaches its peak strength in December (Figure 4), and at this time the current strength increases from north to south. It is still present in January south of 17°N (Figure 2). Both the ship-drift climatology [*Cutler and Swallow*, 1984; *Rao et al.*, 1989, 1991] and hydrographic data [*Shetye et al.*, this issue] support the existence of this southwestward flow, as well as its increase in strength to the south.

3.2. Processes

Figures 5-7, analogous to Figures 2-4 for the main run, illustrate the spatial and temporal structures of each of the process solutions defined in section 2.4. Figures 5a-5d present horizontal plots of their surface circulation and dynamic-height fields. Figures 6a-6c show depth-time plots of the EICC alongshore current at 16°N, 12°N, and 8°N. Figure 7 provides annual curves of the EICC surface current at 16°N, 12°N, and 8°N for the four process solutions and for the main run.

3.2.1. Local alongshore winds. Solution LA is unique among the process solutions in that it is trapped against the western boundary of the basin (Figure 5a), the weak current reversals offshore being due to horizontal mixing, as in the western boundary current of *Munk*'s [1950] solution [*McCreary and Kundu*, 1985; *Shankar et al.*, this issue]. Consistent with its being forced by local alongshore winds, the strength and direction of the surface EICC closely follow the alongshore wind stress, attaining maximum speeds in January and July. Owing to the southward propagation of coastal Kelvin waves along the Indian coast, d develops a tilt to balance the wind stress (Figure 5a), and the amplitude of the EICC increases to the south (Figures 6 and 7). Note that there is flow across the western boundary

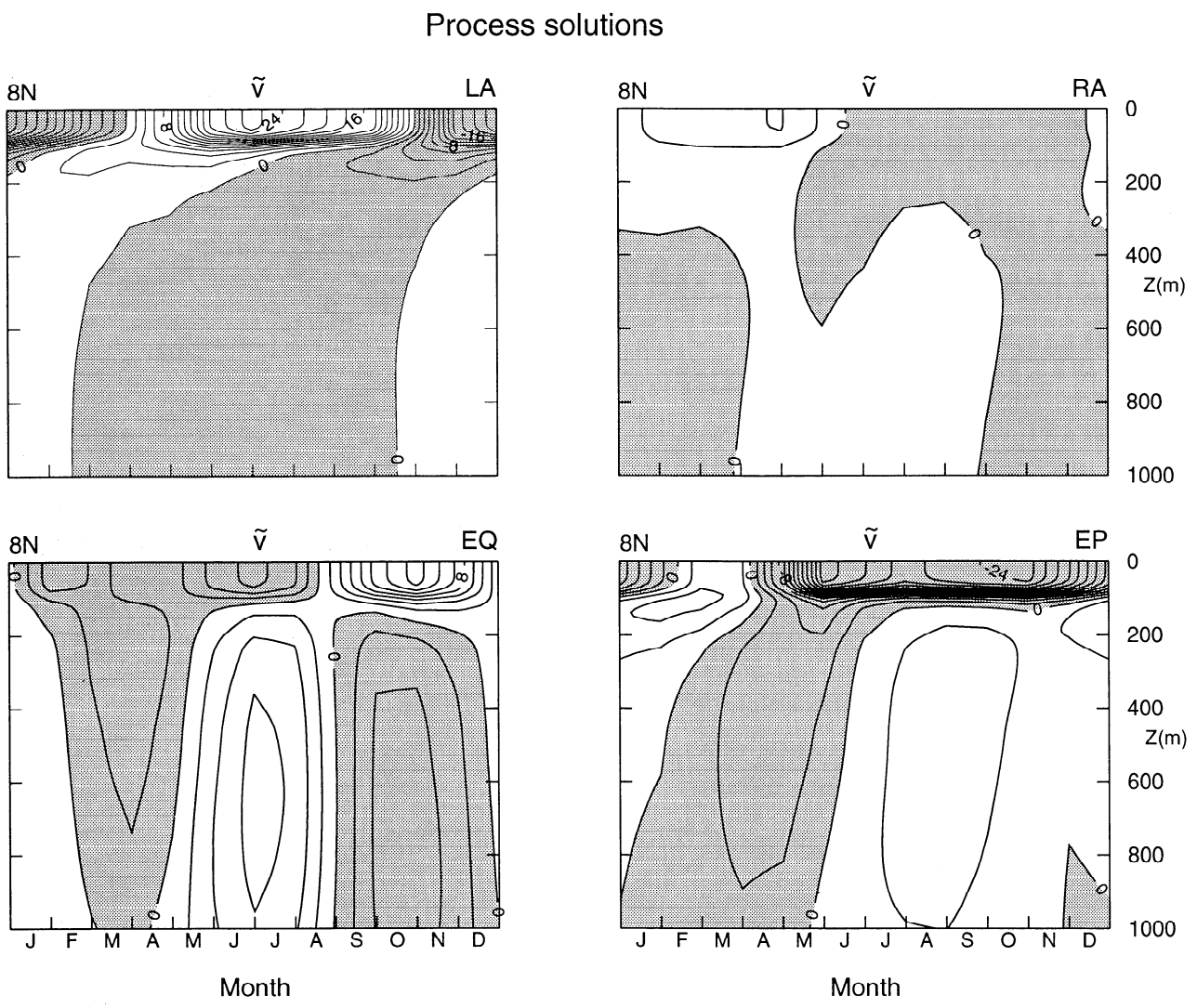

Figure 6c. Same as Figure 6a, except at 8°N. In contrast to their counterparts at 12°N (Figure 6b), solution LA has a somewhat larger amplitude, whereas solution RA is somewhat weaker. Solution EQ has a vertical structure like that of an $n = 2$ baroclinic mode from April to December; this signal results primarily from the propagation of Rossby waves from the eastern boundary rather than from the radiation of Kelvin waves around the perimeter of the basin. Solution EP is dominated by strong, southward surface flow throughout the year, except in February and March.

(most visible in Figure 5a, July and January); this flow is a geostrophic current in balance with the slope in d, which exists because LA, by definition, contains no Ekman drift. Finally, the EICC is confined largely to the surface mixed layer with only weak subsurface flow (Figures 6a–6c, top left). All of these properties, including the absence of significant subsurface flow (a Coastal Undercurrent), agree with those of solutions forced by idealized alongshore winds along a western ocean boundary [*McCreary and Kundu*, 1985]. The fact that there is any subsurface flow at all results from Kelvin-wave energy propagating downward, as well as southward [*Romea and Allen*, 1983], but at the low frequencies of interest here the angle of descent is very small.

It is worth noting that solution LA is very similar to its analytic counterpart in *Shankar et al.* [this issue], as it should be. This is evident from a comparison of Figures 6a–6c (top left) with *Shankar et al.* [this issue, Figure 5]. The two solutions differ in that the EICC in the numerical solution is weaker by about 25% and extends somewhat deeper into the water column. These differences are due to the downward propagation of energy in the numerical solution, a process that is filtered out of the analytic model.

3.2.2. Remote alongshore winds. The dynamics of solution RA differ from those of LA in that, after the coastal currents are generated, they propagate offshore from the eastern ocean boundary as a packet of Rossby waves. Consider the band of low d that appears along the eastern boundary of the Bay in November, increases to its maximum strength in January, and is present until May (Figure 5b). It is generated by

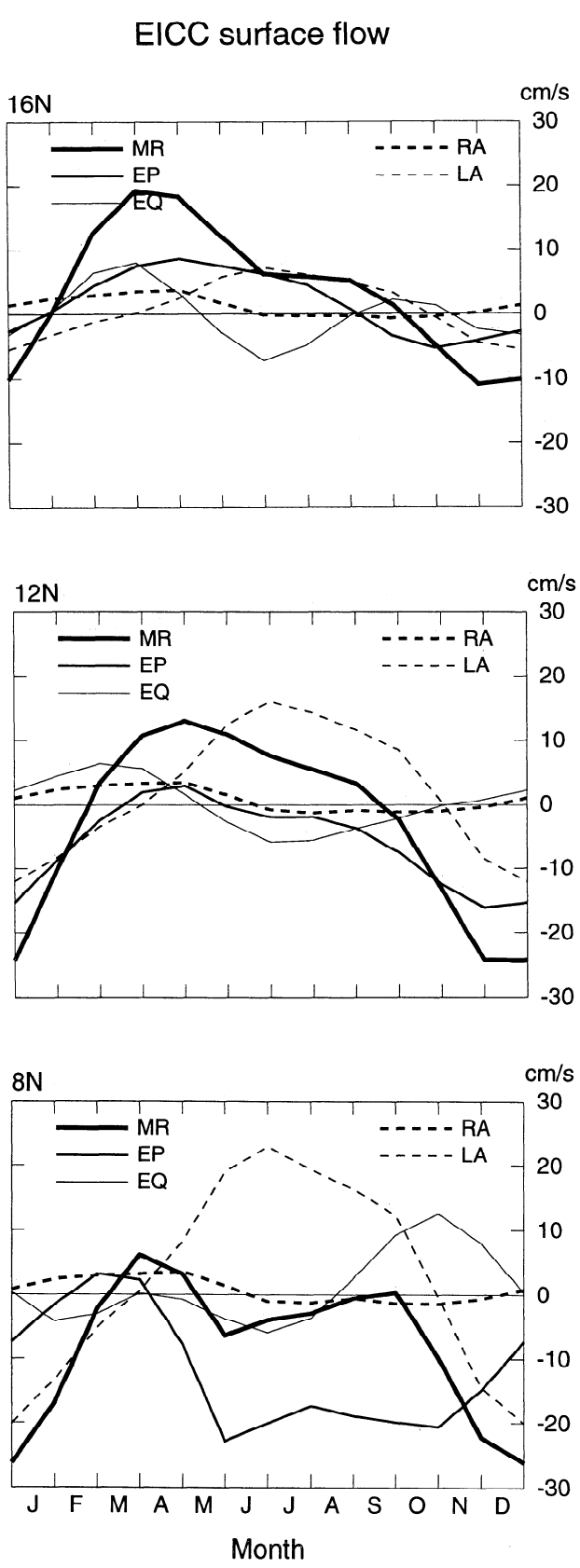

Figure 7. Time plots showing the contribution of each process solution to the average EICC surface velocity at 16°N, 12°N, and 8°N. Solutions LA, EQ, and EP all contribute significantly to the EICC at various times of the year. Solution RA, the weakest contributor overall, provides northward flow from December through June.

upwelling-favorable winds adjacent to the eastern and northeastern boundaries of the Bay (Figure 1, November to March). Analogous to solution LA during the Southwest Monsoon, these winds cause d to slope downward toward the north along the eastern boundary, produce a geostrophic flow out of the basin, and drive an anticyclonic circulation around the perimeter of the Bay via the propagation of coastal Kelvin waves. As time passes, however, the region propagates westward as a packet of Rossby waves, separating completely from the eastern boundary in May with the onset of the Southwest Monsoon (Figure 5b, May); remnants of this region are still visible in the following September as an area of relatively low d in the western basin (Figure 5b, September).

An analogous band of positive d and northward current, driven by downwelling-favorable winds along the eastern boundary (Figure 1, May to September), develops in May and continues through October. In striking contrast to its negative-d counterpart, however, this region does not extend completely around the perimeter of the Bay but, rather, ends abruptly in the northern basin. This difference is due to the presence of upwelling-favorable winds along the northern coast during the Southwest Monsoon (Figure 1), which drive a geostrophic outflow that effectively cancels the inflow generated farther to the south. Indeed, solution RA never has a significant impact on the EICC during the summer because of this cancellation (Figures 6 and 7). With the collapse of the Southwest Monsoon in October the region of high d separates from the eastern boundary and subsequently propagates westward across the basin; it can still be detected in the following July as a "bump" of high d adjacent to the western boundary centered near 15°N (Figure 5b).

3.2.3. Equatorial forcing. Solution EQ, which consists of a packet of Rossby and Kelvin waves remotely forced from the equator, is characterized by strong flows in the eastern basin that extend around the perimeter of the Bay. There are two extreme events of this sort during the year as follows: one pulse of negative d and anticyclonic flow beginning in January and peaking in March, and another pulse of positive d and cyclonic flow beginning in May and peaking in July (Figure 5c). Two weaker events are a second negative-d pulse in September and October, and an anomalously positive one in November and December (Figures 5c and 6a). (See *McCreary et al.* [1993] for a discussion of the processes that generate these pulses.) The gradual propagation of the positive pulse across the basin as a packet of Rossby waves is particularly evident in Figure 5c, eventually becoming the area of relatively high d in the western basin in the following March. Indeed, the arrival of this positive band at the east coast of Sri Lanka in September drives a northward coastal current in the fall, and it is the strongest of any of the flows caused by this mechanism throughout the year (Figures 5c, 6, and 7). Similarly, but less evident, the pulse

of negative d propagates across the basin, becoming the band of low dynamic height that intersects the Indian coast near 10°N in September (Figure 5c); it generates a southward EICC, and this flow is the reason that the semiannual component of the surface current appears less prominent at 12°N than at 16°N (Figures 6a, 6b, and 7).

Strong deep currents are associated with EQ, consistent with its being a remotely forced signal (Figures 6a–6c, bottom left). Indeed, at 16°N and 12°N the deep currents associated with the two major events are shifted in phase from the surface currents in such a way that phase propagates upward in time, another indication that they are remotely forced signals. In contrast, the vertical structure at 8°N is much like that of a pure $n = 2$ baroclinic mode from April through December, with little indication of vertical propagation (Figure 6c); this is because these signals result primarily from Rossby-wave propagation across the southern basin rather than from Kelvin-wave radiation around its perimeter.

Another property of solution EQ evident in Figures 6a–6c is that its semiannual component is relatively larger than it is for the other process solutions. *Jensen* [1993] and *Clarke and Liu* [1993] have noted a similar property in their solutions, attributing it to an equatorial resonance of the $n = 2$ mode at the semiannual cycle. A similar resonance occurs in our model.

3.2.4. Ekman pumping. Solution EP is forced throughout the interior of the Bay by the Ekman pumping velocity $\mathcal{E}$ [see *Shankar et al.*, this issue]. The following two distinctive patterns of $\mathcal{E}$ are evident in Figure 1: $\mathcal{E}$ is negative throughout the northern Bay during the Northeast Monsoon and continuing through April, and it is positive in the western basin, particularly in the southwestern corner, during the Southwest Monsoon and continuing through December. In response to the former forcing, d increases in the northeastern basin until May, there is an anticyclonic circulation about this region, and northeastward flow in the EICC (Figure 5d, January to May, and Figure 7). In response to the latter, d shallows in the western basin beginning in May, resulting in a cyclonic circulation that typically is most intense just offshore from Sri Lanka (Figure 5d, May to January). By definition, EP is the only process solution that contains Ekman drift, and so it is the only one in which current arrows cross isolines of dynamic height (Figure 5d); this crossing is most evident during the Southwest Monsoon, an indication of the intensity of the winds during this season.

Note that there is a significant slope in d along the coast of India and Sri Lanka, downward to the south, from July through November. In contrast to solution LA, this slope exists in order to create an alongshore pressure gradient that balances the mixing terms in the alongshore momentum equations since effects due to the alongshore winds are filtered out of the response. Solutions LA and EP are the only process solutions that develop a significant coastal dynamic-height slope. Both solutions contribute to the large slope present in the main run during the summer (Figure 2). See *Shankar et al.* [this issue, section 4.2], for a further discussion of effects due to various aspects of $\mathcal{E}$.

Just as for solution EQ, the EICC for solution EP also has significant currents below the mixed layer (Figures 6a–6c, bottom right), a consequence of the solution being dominated by contributions from the $n = 1$ and $n = 2$ modes [*Shankar et al.*, this issue]. They also exhibit upward phase propagation, with currents appearing first at depth and rising to the surface several months later.

As for solution LA, solution EP is similar in the numerical and analytical models. The interior circulations for each solution are shown in Figure 5d and given by *Shankar et al.* [this issue, Figure 2a]. The two solutions compare well everywhere, except along the coasts of India and Bangladesh, since the circulation plotted in their Figure 2a does not include the western boundary current (which is plotted by *Shankar et al.* [this issue, Figure 2b]). Away from the western boundary region the primary difference between the two solutions is that the analytic solution is not as smooth as the numerical one, a consequence of horizontal mixing being neglected in its interior response. The EICCs for each solution are shown in Figures 6a–6c (bottom right) and by *Shankar et al.* [this issue, Figure 3a]. Generally, there is good agreement between the structure of the two EICCs, but the numerical one has a somewhat weaker amplitude. This difference is due to horizontal mixing in the numerical model, which dampens Rossby waves as they propagate across the basin.

3.3. EICC Dynamics

To conclude this section, we assess the relative contributions of each process solution to prominent features of the EICC annual cycle. Figure 7 is particularly useful in this regard for the surface flows because the process solution curves sum to the main-run curve, thereby providing a quantitative measure of their contribution. Figures 6a–6c allow a visual assessment of the subsurface flows.

3.3.1. Northward surface flow. Along the Indian coast (Figure 7, top and middle) all four processes contribute to the northeastward surface flow at different times during the spring and summer. Solution RA is the only process that is positive during the winter, and it accounts for the onset of northeastward flow at the beginning of February in northern India (Figure 7, top). Subsequently, solutions EQ, EP, and LA develop northeastward contributions, attaining their peak flows in March, May, and July, respectively. Note that the relative contribution of solutions EP and LA differ considerably at 12°N and 16°N, EP being larger at 16°N where the anticyclonic gyre is better developed (Figure 5d), and LA being larger at 12°N since its amplitude increases to the south (Figure 5a). Note also that the

rapid decrease in strength of the EICC after April is largely due to EQ, which provides a negative contribution from May through August (Figure 5c).

Off Sri Lanka the weak northward surface current in March and April is generated by solutions RA and LA, as well as the weak reversal of EP at that time (Figure 7, bottom). However, the most striking aspect of the flow is the lack of significant northward flow from May to October, in spite of the large positive contribution from solution LA and, to a lesser extent, solution EQ (Figure 7). This lack is caused by the large negative contribution from EP (Figure 5d), which is driven by the strong positive Ekman pumping velocity east of Sri Lanka that is present for so much of the year (Figure 1).

3.3.2. Southward surface flow. Solutions EP and LA are the causes of the wintertime southward flow along both India and Sri Lanka, with EQ making a weak contribution at 16°N (Figure 7). It is noteworthy that due to the contribution of solution EP, southward flow begins toward the end of September at all locations, even though the local winds do not shift to northeasterly until November. Off Sri Lanka the circulation from solution EP remains roughly constant ($\simeq -20$ cm s^{-1}) during the onset; thus the onset is triggered by the weakening of the alongshore winds (and hence a decrease in the positive contribution of LA), a conclusion also reached by *McCreary et al.* [1993].

3.3.3. Subsurface currents. Figures 6a and 6b show that the cause of the summertime Coastal Undercurrent is not solution LA, which only has a weak, subsurface counterflow. Rather, solution EQ provides the largest contribution to the southwestward flow in the depth range of the Coastal Undercurrent in May and June, whereas solution EP is the dominant component later in the season. Remote equatorial forcing was suggested by *McCreary et al.* [1993] as the cause of the Coastal Undercurrent along the east coast of India in their solution during May; the undercurrent was not present later in the season, probably due to the lack of vertical resolution in their $2\frac{1}{2}$-layer model. A Coastal Undercurrent driven by interior Ekman pumping also developed in the solutions of *McCreary and Kundu* [1985], who discuss its dynamics; it is likely that the Coastal Undercurrent in this study exists for similar reasons.

As shown in Figure 4, the curves of transport can differ considerably from those of surface current due to the presence of significant subsurface flows. This is particularly evident along the coast of India, where the transport reverses to flow southwestward during the summer but the surface current does not. A comparison of Figures 6a and 6b shows that this reversal is primarily due to deep, southwestward currents associated with solution EQ.

Recall that along the Indian coast the maximum northeastward transport in the solution is only about half the observed value. The reason for this discrepancy is not clear. Given the strong influence of solution EQ on the EICC transport, a possible cause is errors in the structure or propagation speeds of the remotely forced waves that comprise solution EQ. Imagine, for example, a delay that shifts the EQ plots in Figures 6a and 6b to the right by $1\frac{1}{2}$ months; unshaded regions of solutions EQ and EP will then overlap much more constructively in the spring, thereby increasing the northeastward transport. Distortions of this sort might be induced by the continental shelf, which is necessarily neglected in our model.

4. Discussion

In this paper a linear, continuously stratified model is used to investigate the relative importance of the following four driving mechanisms of the EICC: local alongshore winds, remote alongshore winds, equatorial forcing, and interior Ekman pumping. Effects due to each mechanism are isolated in four process solutions (section 2.4). Properties of these solutions (Figures 5 and 6) agree with those of idealized solutions forced by a single mechanism, indicating that they properly represent the response to each forcing type. Figure 7 allows the relative contributions of each process to be assessed both visually and quantitatively.

Generally, our solutions confirm the conclusions of the earlier studies mentioned in the introduction. Local alongshore winds are a very important forcing mechanism throughout the year. As suggested by *McCreary et al.* [1993], it is the collapse of these winds at the end of the Southwest Monsoon that accounts for the generation of a southward EICC in the fall and winter along the southern coast (Figure 7, bottom). Interior Ekman pumping is an equally important process and, as suggested by *Shetye et al.* [1993], it contributes prominently to the northeastward surface EICC in the spring along the northern coast (Figure 7, top); it also prevents the EICC from flowing northward during the summer off Sri Lanka (Figure 7, bottom). Equatorial forcing is also influential, as suggested by *Yu et al.* [1991] and *Potemra et al.* [1991]; it contributes to northeastward flow in the EICC in the spring, weakens it in the summer (Figure 7, top and middle), and delays the onset of southward flow off Sri Lanka in the fall (Figure 7, bottom). Finally, although the contribution of remote alongshore winds is relatively weak throughout the year, these winds do contribute to the onset of the northeastward EICC in the spring, as suggested by *McCreary et al.* [1993] (Figure 7, top).

In conclusion, we believe that our dynamically simple model has identified the basic processes that account for much of the wind-driven circulation throughout the Bay of Bengal. Because of its simplicity, however, the model is limited in a number of obvious ways. For one thing, as noted above, the model surely misrepresents to some degree the structure and propagation speeds of remotely forced signals, and this discrepancy may distort transport values of the model EICC. For another,

its linearity prevents the generation of instabilities, but eddies are a prevalent feature in the interior of the Bay [*Babu et al.*, 1991; *Shetye et al.*, 1993]. Finally, the model lacks a surface mixed layer that can respond to the large, fresh water influx into the Bay. The use of more sophisticated models, which can overcome these and other limitations, will be required in order to develop a complete understanding of the region's complex circulations.

Acknowledgments. Julian McCreary and Weiqing Han were supported by NSF grant OCE-92-03916 and by ONR grant N00014-90-J-1054. D. Shankar and Satish Shetye were supported by the Department of Ocean Development. The programming support of Kevin Kohler is greatly appreciated.

References

Anderson, D. L. T., D. J. Carrington, R. Correy, and C. Gordon, Modelling the variability of the Somali Current, *J. Mar. Res.*, *49*, 659–696, 1991.

Babu, M. T., S. P. Kumar, and D. P. Rao, A subsurface cyclonic eddy in the Bay of Bengal, *J. Mar. Res.*, *49*(3), 403–410, 1991.

Clarke, A. J., and X. Liu, Observations and dynamics of semiannual and annual sea levels near the eastern equatorial Indian Ocean boundary, *J. Phys. Oceanogr.*, *23*, 386–399, 1993.

Cutler, A. N., and J. C. Swallow, Surface currents of the Indian Ocean (to 25°S, 100°E), *Tech. Rep.*, 187, 8 pp., Institute of Oceanogr., Wormley, England, 1984.

Hellerman, S., and M. Rosenstein, Normal wind stress over the world ocean with error estimates, *J. Phys. Oceanogr.*, *13*, 1093-1104, 1983.

Jensen, T. G., Equatorial variability and resonance in a wind-driven Indian Ocean model, *J. Geophys. Res.*, *98*, 22,533–22,552, 1993.

Levitus, S., Climatological atlas of the world ocean, *NOAA Prof. Pap. 13*, 173 pp., U. S. Govt. Print. Off., Washington, D.C., 1982.

McCreary, J. P., Modelling wind-driven ocean circulation, *Tech. Rep. HIG-80-3,* 64 pp., Hawaii Inst. of Geophys., Honolulu, 1980.

McCreary, J. P., A linear stratified ocean model of the coastal undercurrent, *Philos. Trans. R. Soc. London A*, *302*, 385-413, 1981.

McCreary, J. P., and P. K. Kundu, Western boundary circulation driven by an alongshore wind: With application to the Somali Current system, *J. Mar. Res.*, *43*, 493–516, 1985.

McCreary, J. P., P. K. Kundu, and R. L. Molinari, A numerical investigation of dynamics, thermodynamics, and mixed-layer processes in the Indian Ocean, *Prog. Oceanog.*, *31*, 181-224, 1993. (Correction, *Prog. Oceanogr.*, *33*, after pg. 248, 1994.)

Moore, D. W., and J. P. McCreary, Excitation of intermediate frequency equatorial waves at a western ocean boundary: With application to observations from the Indian Ocean, *J. Geophys. Res.*, *95*, 5192-5231, 1990.

Munk, W. H., On the wind-driven ocean circulation, *J. Meteorol.*, *7*, 79-93, 1950.

Potemra, J. T., M. E. Luther, and J. J. O'Brien, The seasonal circulation of the upper ocean in the Bay of Bengal, *J. Geophys. Res.*, *96*, 12,667-12,683, 1991.

Rao, R. R., R. L. Molinari, and J. F. Festa, Evolution of the climatological near-surface thermal structure of the tropical Indian Ocean, 1, Description of mean monthly mixed-layer depth and sea-surface temperature, surface-current, and surface meteorological fields, *J. Geophys. Res.*, *94*, 10,801–19,815, 1989.

Rao, R. R., R. L. Molinari, and J. F. Festa, Surface meteorological and near-surface oceanographic atlas of the tropical Indian Ocean, *NOAA Tech. Memo. ERL AOML-69*, NOAA Atl. Oceanogr. and Meteorol. Lab., Miami, Fla., 1991.

Romea, R. D., and J. S. Allen, On vertically propagating coastal Kelvin waves at low latitudes, *J. Phys. Oceanogr.*, *13*, 1241–1254, 1983.

Shankar, D., J. P. McCreary, W. Han, and S. R. Shetye, Dynamics of the East India Coastal Current, 1, Analytic solutions forced by interior Ekman pumping and local alongshore winds, *J. Geophys. Res.*, this issue.

Shetye, S. R., S. S. C. Shenoi, A. D. Gouveia, G. S. Michael, D. Sundar, and G. Nampoothiri, Wind-driven coastal upwelling along the western boundary of the Bay of Bengal during the Southwest Monsoon, *Cont. Shelf Res.*, *11*, 1397-1408, 1991.

Shetye, S. R., A. D. Gouveia, S. S. C. Shenoi, D. Sundar, G. S. Michael, and G. Nampoothiri, The western boundary current of the seasonal subtropical gyre in the Bay of Bengal, *J. Geophys. Res.*, *98*, 945-954, 1993.

Shetye, S. R., A. D. Gouveia, D. Shankar, S. S. C. Shenoi, P. N. Vinayachandran, D. Sundar, G. S. Michael, and G. Nampoothiri, Hydrography and circulation in the western Bay of Bengal during the Northeast Monsoon, *J. Geophys. Res.*, this issue.

Yu, L., J. J. O'Brien, and J. Yang, On the remote forcing of the circulation in the Bay of Bengal, *J. Geophys. Res.*, *96*, 20,449-20,454, 1991.

W. Han and J. P. McCreary, Oceanographic Center, Nova Southeastern University, 8000 N. Ocean Dr., Dania, FL 33004. (e-mail: jay@ocean.nova.edu)

D. Shankar and S. R. Shetye, National Institute of Oceanography, P. O. Box NIO, Dona Paula, Goa 403 004, India. (e-mail: shetye@bcgoa.ernet.in)

(Received August 7, 1995; revised January 3, 1966; accepted January 24, 1996.)